Journal of Luminescence 215 (2019) 116618

Contents lists available at ScienceDirect

Journal of Luminescence

journal homepage: www.elsevier.com/locate/jlumin

Controlling luminescence and quenching mechanisms in subnanometer multilayer structure of europium titanium oxide thin films

Per-Anders Hansen[a,*], Cecilie S. Granerød[b], Øystein Prytz[b], Ola Nilsen[a]

[a] Department of Chemistry, Centre for Materials Science and Nanotechnology, University of Oslo, Sem Sælandsvei 26, 0371 Oslo, Norway
[b] Department of Physics, Centre for Materials Science and Nanotechnology, University of Oslo, P.O. Box 1048 Blindern, N-0316 Oslo, Norway

ABSTRACT

We have investigated how layered structures of TiO_2 and Eu_2O_3 on the subnanometer scale control the optical absorption, energy transfer, emission and quenching mechanisms in sensitized lanthanide luminescence systems. By using atomic layer deposition (ALD) as a tool for designing materials with sub nanometer precision, we have been able to make structures ranging from separate $(TiO_6)^{8-}$ clusters to bulk TiO_2, and series of samples showing transitions from 3D to 2D energy migration. Photoluminescence, excitation and decay measurements have been used alongside transmission electron microscopy (TEM) to investigate how the different structures affect the luminescence. We show that it is possible to drastically suppress concentration quenching compared to solid solutions by designing materials as multilayered structures that confines energy migration in 2D planes. This allows for application of higher concentrations of lanthanides and more defected structures, also enabling use of less pure reactants during synthesis.

1. Introduction

Luminescent materials based on lanthanides is a well-developed field with respect to materials [1], mechanisms [2] and applications like lighting [3], laser [4], optoelectronics [5], optical markers for nanobiology [6] and solar cells [7–9]. Inorganic phosphors have the advantage of being resistant to harsh conditions like deep UV, high and cryogenic temperatures, high electric fields and high laser intensities compared to organic and molecular phosphors.

Inorganic phosphors are generally based on a luminescent ion in a crystalline host matrix, often sensitized by a second type of ion or by the matrix itself. The ions are usually randomly distributed, which is sufficient in simple luminescent systems where only one or two types of atoms interact. In such systems it is enough that the concentration of active ions is kept low to avoid concentration quenching effects [10]. However, there is a current shift in interest towards more advanced optical systems, requiring interactions between three or more different types of ions. Examples are sensitized down conversion [11] or up conversion [12]. For such systems, simple random distribution is not sufficient as the optical properties and concentration of one ion may end up quenching another ion in a later stage in the luminescence pathway.

Multishell nanoparticles have been shown to offer a unique ability to separate different optically active ions in layers, allowing much better control of interaction pathways. Sensitization of one ion can be accomplished while avoiding detrimental interaction with a second or third ion. This has recently led to highly efficient up conversion systems based on step-wise interaction between up to 4 lanthanide ions [13]. However, such multishell structures are limited to those materials that can be easily synthesized in such a manner, which are mostly fluorides like $NaYF_4$ [14]. Creating complex multishell structures of common optical materials like oxide garnets, oxysulfides, halophosphates and silicates is not trivial.

We have recently shown that it is possible to create multilayered structures of luminescent oxides with layer thicknesses smaller than 0.4 nm using atomic layer deposition (ALD) [15,16]. Multilayers of amorphous TiO_2 and Eu_2O_3 showed almost identical optical and luminescence properties as a homogeneous mixture of the two oxides. This indicated that ALD can be used to design layers thinner than the interaction distances between optically active ions. Deposition of nearly all lanthanide oxides can similarly be deposited by ALD [17], and the types of materials that can be deposited range from inorganic oxides, halides, sulphides and nitrides [18] to organic-inorganic hybrids [19]. This material flexibility and thickness control makes ALD very well suited for complex multicomponent optical systems [20]. In the current work, we aim at investigating how the subnanometer multilayer structures of TiO_2 and Eu_2O_3 affect the absorption, transfer and quenching mechanisms.

2. Experimental

The depositions were done by ALD and details of the processes are

* Corresponding author.
E-mail address: p.a.hansen@kjemi.uio.no (P.-A. Hansen).

https://doi.org/10.1016/j.jlumin.2019.116618
Received 11 August 2018; Received in revised form 13 June 2019; Accepted 9 July 2019
Available online 10 July 2019

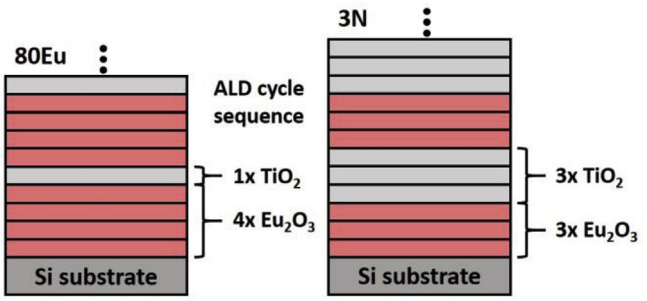

Fig. 1. Illustration of the two sample series *x*Eu and *x*N illustrated with 80Eu and 3 N, respectively. 80Eu is 80% Eu_2O_3 cycles and 20% TiO_2 cycles. 3 N is a multilayer structure of 3 sequential Eu_2O_3 cycles followed by 3 sequential TiO_2 cycles.

described in our earlier works [15,16]. One Eu_2O_3 cycle is made up by one $Eu(thd)_3$ pulse followed by an ozone pulse, thd = 2,2,6,6-tetramethyl-3,5-heptanedionate. Likewise, one TiO_2 cycle is made up of one $TiCl_4$ pulse followed by an H_2O pulse. All films have a total film thickness of about 80 nm. Two sample series are investigated in this work, illustrated in Fig. 1. These two series investigates the luminescence properties as a function of Eu_2O_3/TiO_2 cycle ratio, and Eu_2O_3/TiO_2 layer thicknesses, respectively. For both series, the first cycle and the first layer is always Eu_2O_3.

In the first set, the stoichiometric ratio between Eu_2O_3 and TiO_2 is varied. This is done by varying the number of Eu_2O_3 and TiO_2 cycles. These samples are named *x*Eu where *x* is the percentage of Eu_2O_3 cycles, i.e. 80Eu is repeating supercycles of 4 Eu_2O_3 cycles followed by 1 TiO_2 cycle. These cycles are sequenced so that they give the most homogeneous distribution, i.e. the supercycle sequence of 60Eu is Eu-Eu-Ti-Eu-Ti, not Eu-Eu-Eu-Ti-Ti. As the growth rate of Eu_2O_3 is lower than that of TiO_2, less europium is deposited than its pulsed percentage. All *x*Eu samples are amorphous according to XRD, apart from 10Eu and 20 Eu where XRD detects an increasing amount of anatase with increasing TiO_2 content [16].

In the second set. The cycle ratio of 50Eu is kept constant, while the number of sequential Eu_2O_3 and TiO_2 cycles is varied. These are named *x*N where *x* represents the number of sequential cycles, i.e. the supercycle sequence of 4 N is Eu-Eu-Eu-Eu-Ti-Ti-Ti-Ti. This set investigates how the luminescence changes when the material is changed from a homogeneous mixture (1 N) to a multilayer structure with individual Eu_2O_3 and TiO_2 layer thicknesses up to 2.1 nm. In our previous work, we determined the superlayer structure, i.e. one Eu_2O_3 layer plus one TiO_2 layer, was 0.6, 1.6 and 3.9 nm for the 10 N, 20 N and 50 N samples [15]. In addition, all *x*N samples are amorphous according to XRD. Note that 50Eu and 1 N has the same cycle sequence.

Luminescence (PL) and excitation (PLE) measurements was done on two different experimental configurations. PL for *x*N samples [15] (Fig. 2 A) and PLE for both *x*Eu and *x*N samples (Fig. 5) was measured using an Edinburgh Instruments FLS920 fluorescence spectrometer with a 450 W Xe lamp as excitation source and a Hamamatsu R928 PMT for detection. PL for *x*Eu samples [16] (Fig. 2B and C) was measured using a 325 nm He–Cd laser and a USB4000 spectrometer (OceanOptics). This was due to an upgrade of the equipment in between the *x*Eu and *x*N series. Relative quantum efficiencies was estimated by dividing the integrated luminescence signal in the 550–750 nm range by the UV absorbance. The UV absorbance on silicon samples was calculated taking into account the refractive indexes and extinction coefficients of the film and silicon substrate from ellipsometry (VASE Ellipsometer, J. A. Woollam), explained in detail in our previous two works [15,16], and the incident angle of the UV excitation. PL decay measurements were performed with an optical parametric oscillator (OPO) system (Opotek HE 355 II) pumped by the third harmonic of a Nd:YAG laser as excitation source. The OPO system was set to 355 nm and a repetition

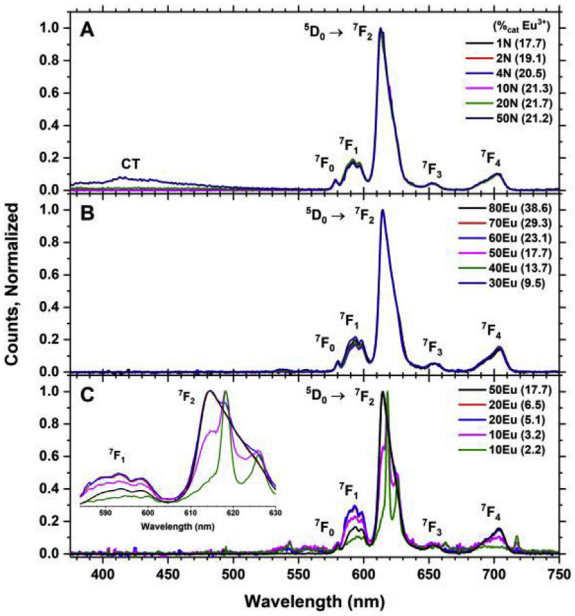

Fig. 2. (A) PL of multilayered films showing titanate CT emission only for N = 50, λ_{ex} = 300 nm, (B) PL of 30-80Eu showing identical emission spectra between these samples, λ_{ex} = 325 nm, (C) PL of 10-20Eu samples compared to 50Eu showing an increasing amount of Eu^{3+} doped anatase, λ_{ex} = 325 nm.

rate of 20 Hz. The decay was recorded with the same equipment used for the excitation measurement.

Transmission Electron Microscopy (TEM) investigations of the samples were conducted after standard sample preparation techniques, by cutting, manual grinding, and polishing. Final thinning was done with a Gatan PIPS II ion mill using Ar ions, with gradually decreasing voltages and angles and increasing polishing time. Plasma cleaning with a Fishione Model 1020 for ca. 5 min was applied prior to the TEM experiments. Scanning Transmission Electron Microscopy (STEM) was performed with an FEI Titan G2 60–300 kV TEM, equipped with a CEOS probe-corrector. The microscope was operated at 300 kV with a convergence angle of 31 mrad, where Annular Dark Field (ADF) and High Angle Annular Dark Field (HAADF) imaging were done with collection angles 21.5–99 and 99–200 mrad, respectively.

Electron Energy-Loss Spectroscopy (STEM-EELS) was performed with a Gatan Quantum965 GIF with 0–21.1 mrad collection angle and a dispersion of 0.25 eV/channel. Acquisitions were performed in spectrum image dual EELS mode with high binning. Dark corrections were applied after the acquisitions, and the spectra were calibrated by the Zero-Loss Peak (ZLP) position. Principal Component Analysis (PCA) has previously been seen to effectively reduce spectral noise [21], and was here applied with 20 components. The background was subtracted from each spectrum by fitting a power-law function below the region of interest.

3. Results

Fig. 2 shows PL spectra of both *x*Eu and layered *x*N samples upon excitation through the TiO_2 CT band, normalized to the $^5D_0 \rightarrow {}^7F_2$ peak. The excitation wavelength was 300 and 325 nm for *x*N and *x*Eu samples, respectively, due to the two different optical configurations used. We verified with several samples that they have identical emission spectra in both configurations, proving that the tools gives comparable results in the context of this work. The emission spectrum from Eu^{3+} is in fact identical for all samples, apart from 10 to 20Eu and 50 N. The 50 N sample show in addition a weak and broad emission in the blue range, originating from the titanate charge transfer (CT) state, while 10-20Eu show an increasing amount of Eu^{3+} doped anatase type emission

in addition to amorphous europium titanium oxide type emission, with increasing titanium oxide contents.

These sample are quite similar in many aspects, 10-20Eu being exceptions due to co-growth of anatase crystallites in addition to the amorphous europium titanium oxide phase; All samples, apart from these two, have a very low surface roughness (RMS < 1 nm) and no crystallites meaning that scattering is negligible, and they are all approximately 80 nm thick [15,16]. However, the refractive index and extinction coefficient vary gradually, meaning that the reflectance and interference patterns in the UV range vary. This complicates direct comparison of the different samples luminescence intensity, as the relative amount of absorbed UV energy differs. We have estimated this relative absorbance in the two samples series, by taking into account n(λ), k(λ), film thickness and the incident angle of the UV sources. This calculation is shown in Eqs. (1)–(5), where A, R_{surf}, R_{int}, l, α, θ_1 and θ_2 are the estimated absorption, reflectance at the air/film and film/silicon interfaces, optical path length, absorption coefficient, incident angle and angle inside film, respectively. This accounts for the amount of UV light absorbed during one pass into the film, reflected from the silicon substrate and another pass to the film surface. Due to the strong absorption of these films, this accounts for more than 99% of the light for xEu < 70.

$$A = (1 - R_{surf})\cdot(1 - e^{-l\alpha})\cdot(R_{int})\cdot(1 - e^{-l\alpha}) \quad (1)$$

$$R_{surf} = \left| \frac{n_{air}\cos\theta_1 - n_{film}\sqrt{1 - \frac{n_{air}}{n_{film}}\sin\theta_1}}{n_{air}\cos\theta_1 + n_{film}\sqrt{1 - \frac{n_{air}}{n_{film}}\sin\theta_1}} \right|^2 \quad (2)$$

$$R_{int} = \left| \frac{n_{film}\cos\theta_2 - n_{Si}\sqrt{1 - \frac{n_{film}}{n_{Si}}\sin\theta_2}}{n_{film}\cos\theta_2 + n_{Si}\sqrt{1 - \frac{n_{film}}{n_{Si}}\sin\theta_2}} \right|^2 \quad (3)$$

$$\theta_2 = \sin^{-1}\left(\frac{n_{air}\sin\theta_1}{n_{film}}\right) \quad (4)$$

$$l = \frac{t_{film}}{\cos\theta_2} \quad (5)$$

By integrating the luminescence signal in the 550–750 nm range and dividing it by the calculated relative absorbance, we obtain an estimate of the relative quantum efficiency between the samples. These results are summarized in Fig. 3. For xN samples, the Eu_2O_3/TiO_2 cycle ratio is constant, but the difference in cycle sequence also leads to differences in Eu^{3+} contents. Thus the actual Eu^{3+} content is also plotted for this set (right y-axis). The xEu set is plotted vs $\%_{cat}$ Eu^{3+}, while the xN set is plotted vs the number of sequential cycles in each layer.

For the xEu set, the UV absorbance decreases with decreasing TiO_2 content, apart from for the 10-20Eu samples. This means that the relative absorbance is dominated by the gradual decrease in k(λ). The measured PL intensities has a maximum at 50Eu. However, when taking into account the calculated amount of absorbed UV, the 60Eu has a higher relative efficiency. For the xN set, there is some variation in the amount of absorbed UV, coming from the variation in n(λ) and k(λ) due to variation in Eu^{3+} content.

The decay of both series is shown in Fig. 4. All samples can be fitted with a single exponential function, accounting for more than 90% of the signal of all sample. The non-exponential shape in the very beginning of the data is due to the co-existence of non-equal Eu^{3+} with respect to site symmetry and/or available quenching mechanism. Apart from the anatase component of 10Eu and 20Eu, the site symmetry of Eu^{3+} is unknown in the amorphous phase and might change gradually towards the air/film or film/substrate interfaces due to strain. In particular for the 10Eu sample which contain two emitting phases (anatase and the amorphous phase), it is expected that there will be at least two non-

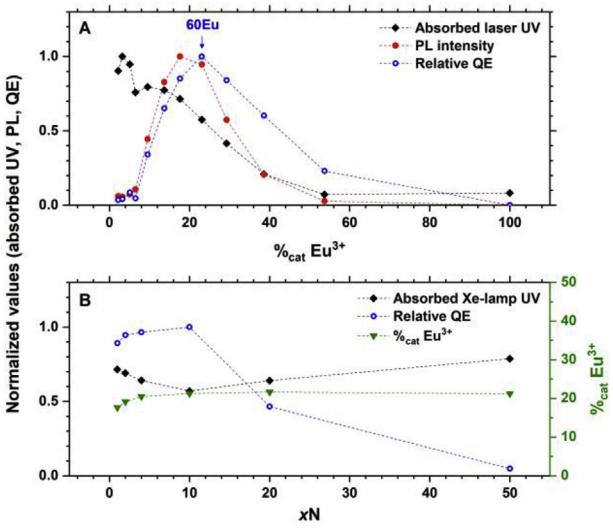

Fig. 3. Relative amount of absorbed UV calculated from n(λ), k(λ), film thickness and angle of incidence (black), integrated emission intensities in the 550–750 nm range (red), relative QE obtained from these two values (blue), and $\%_{cat}$ Eu^{3+} (green), of the xEu (A) and xN (B) sample series. The UV sources was a 325 nm He–Cd laser (A) and 300 nm from a Xe lamp (B).

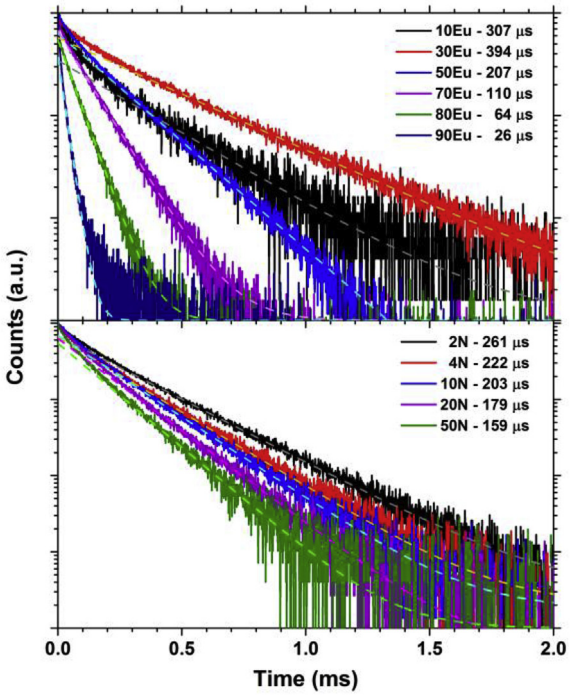

Fig. 4. Decay of the $^5D_0 \rightarrow {}^7F_2$ emission of Eu^{3+} as a function of concentration (top) and multilayer thickness (bottom), excited by 355 nm laser pulses. Fitting is done with a single exponential function.

equal Eu^{3+} that contribute to the lifetime signal. The lifetime decreases with increasing Eu_2O_3 content, which is expected due to concentration quenching effects. The 10Eu sample is an exception to this, as the emission here is mostly from Eu^{3+} in anatase crystallites [16], while the emission in all other samples is due to the amorphous phase. For multilayered samples, however, the reduction in lifetime is much smaller, even for the thickest layers, which are best described as layers of pure TiO_2 and pure Eu_2O_3. The concentration quenching effect is thus much smaller even though the Eu_2O_3 content is 100% within each layer in the multilayer samples.

Fig. 5 show normalized PLE curves for both sample series,

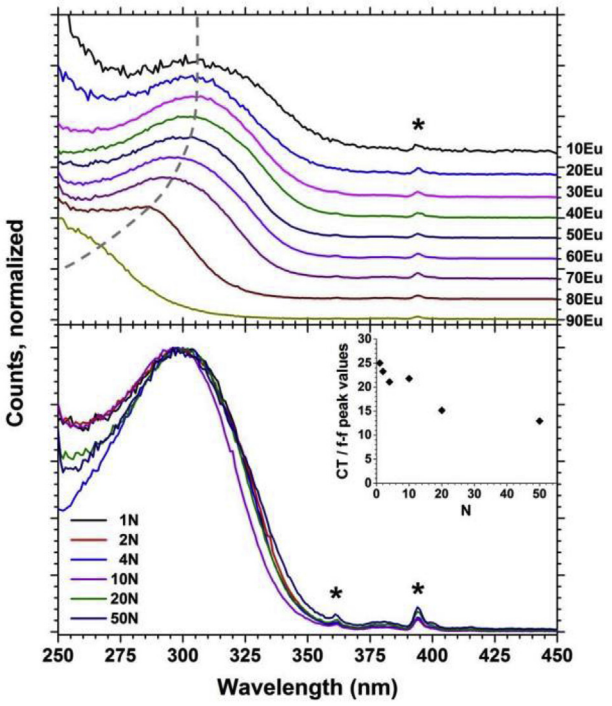

Fig. 5. PLE curves for $^5D_0 \rightarrow {}^7F_2$ emission of Eu^{3+}, $\lambda_{em} = 615$ nm, as a function of Eu_2O_3/TiO_2 cycle ratio (top) and layer thickness (bottom). The broad peak at 300 nm is due to titanate CT transition, while the peaks marked with an asterix are due to f-f transitions on Eu^{3+}. The inset shows the ratio between peak maxima of the CT and 394 nm f-f transitions. The *x*Eu PLE spectra are shifted to better visualize the blueshift of the CT peak for x ≥ 50.

monitoring the $^5D_0 \rightarrow {}^7F_2$ emission at 615 nm. The *x*Eu samples show that the titanate CT peak position is constant for $x \geq 50$, but is blue shifted for lower *x*. In the 50Eu sample, the $(TiO_6)^{8-}$ clusters interact and form a 3D network, obtaining bulk-like properties. At lower concentrations, the interaction between clusters is reduced and their optical properties change from typical of bulk networks towards what is expected for isolated clusters. By comparison, the layered samples show no variation in peak position. This indicates that alternating TiO_2 and Eu_2O_3 cycles is sufficient to produce a 3D network of connected $(TiO_6)^{8-}$ clusters since thicker TiO_2 layers neither shift nor broaden the CT peak. The smaller peaks marked with an asterix stem from f-f transitions on Eu^{3+}. The reason these peaks are so small compared to the CT peak is that the absorption strength of f-f transitions is too weak to fully absorb the excitation light in an 80 nm thin film, while the CT transition absorbs a much larger portion of the incoming light. The inset of Fig. 5 shows that as N increases, producing $^5D_0$ emission becomes less efficient by excitation of the CT state compared to direct excitation of Eu^{3+} even though both n(λ) and k(λ) in addition to the film thickness is similar for all the multi-layered samples [15].

Fig. 6 shows a STEM-HAADF image of the 50 N multilayer structure. Figs. 7 and 8 (explained below) is from the same 50 N sample. The TiO_2 and Eu_2O_3 layers are dark and bright, respectively, as Rutherford scattering mainly dominates scattering to high angles. The HAADF intensity is then approximately proportional to $Z^{1.7-2}$ [22], and hence, heavy Eu atoms appear brighter than Ti. At the interface towards the substrate, a Eu_2O_3 layer is found, whereas the multilayer is terminated with a TiO_2 layer on the surface. In total, 19 Eu_2O_3 layers and 19 TiO_2 layers are identified, across a film thickness of 80 nm. This gives an average layer thickness of 2.1 nm.

Interestingly, as can be seen from the straight red lines, the layers become more uneven and wavy further from the substrate. We can assume that this also occurs along the viewing direction. The STEM sample thickness in the viewing direction is approximately 100 nm.

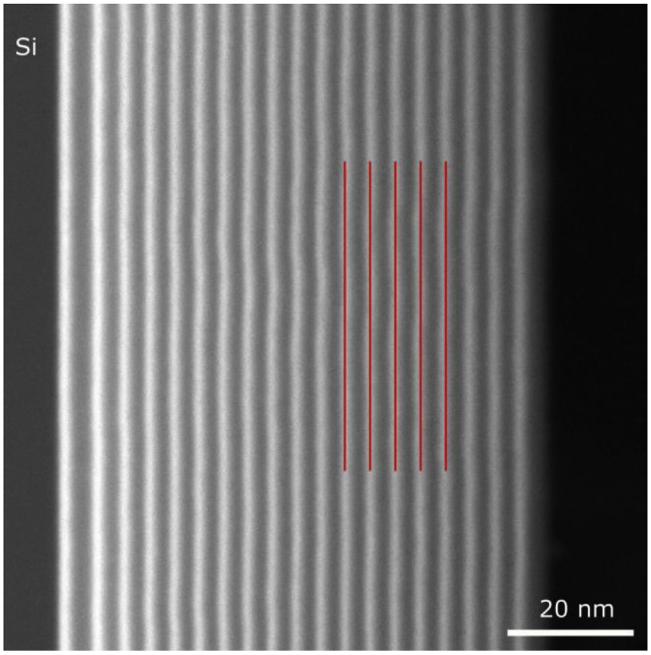

Fig. 6. STEM-HAADF image showing the multilayer structure in the 50 N sample. The red lines are eye guides, showing that the layers become wavier along the film growth direction.

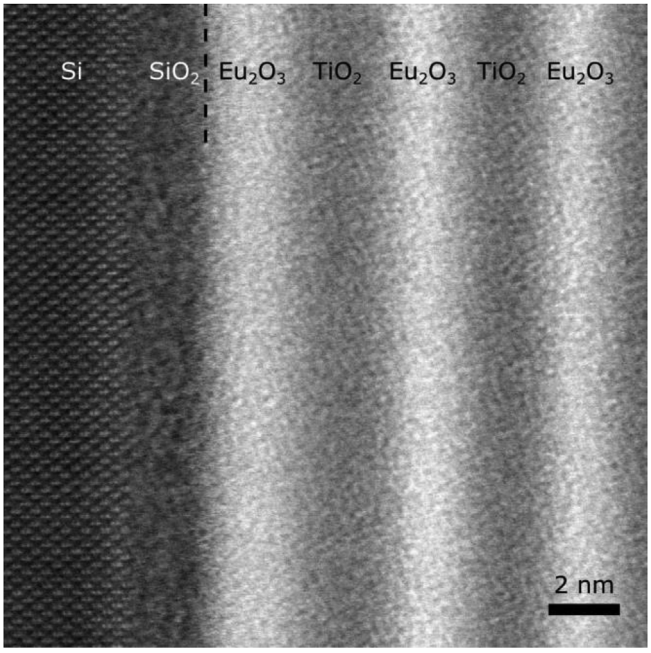

Fig. 7. STEM-ADF close-up of the interface between the multilayer structure and the substrate. An amorphous oxide layer has formed on top of the crystalline Si substrate, whereas the amorphous multilayer structure starts with an Eu_2O_3 layer.

This may also contribute to a blurring of the interfaces, as the image shows that the interfaces of the multilayers are not sharply defined.

A close-up of the interface between the multilayers and the substrate is provided in Fig. 7, where the ADF STEM detector was used. The contrast is more sensitive to screening, and strain also affects the intensity. Here, the Si substrate is atomically resolved, whereas an amorphous SiO_2 layer is seen on top of the crystalline Si. This was confirmed with both Energy-Dispersive X-ray Spectroscopy (EDS) as well as EELS (both not shown). Furthermore, the first layers close to the

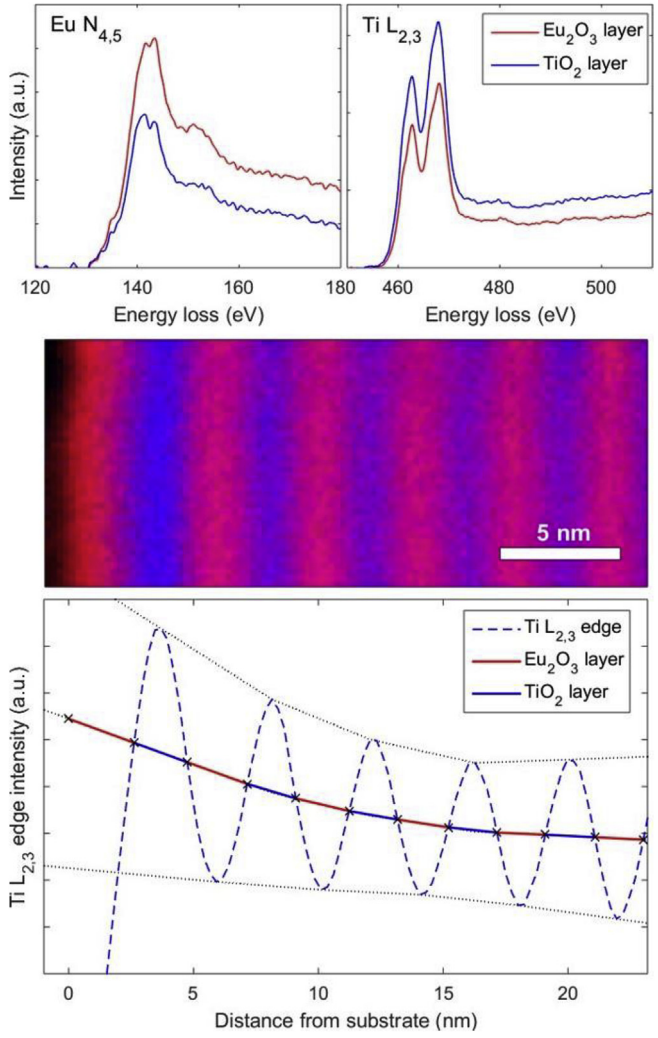

Figure 8. (Top) STEM-EELS results of the Eu N4,5 and Ti L2,3 edges measured in Eu_2O_3 and TiO_2 layers, showing both Eu and Ti signal within both layers. (Middle) STEM-EELS mapping of Eu edge (red) and Ti edge (blue). (Bottom) Line profile of STEM-EELS Ti L2,3 edge across the multilayer structure to obtain film thicknesses.

substrate are shown as alternating Eu_2O_3/TiO_2 layers, also here showing diffuse interfaces.

The composition of the multilayer structure has been investigated further by EELS. This is shown in Fig. 8, where the Eu $N_{4,5}$ and Ti $L_{2,3}$ energy loss edges have been used. STEM-EELS from the middle of the two first films show that the first Eu_2O_3 layer also contains Ti, and that the first TiO_2 layer contains Eu. Hence, the layers appear somewhat mixed, which could be explained by the uneven interfaces between the films. A complete mapping of the layers close to the substrate is also shown, showing that the two first layers are thicker and more distinct than the following layers. This correlation between film thickness and composition also supports that the interfaces are not completely straight, which blur the spatial resolution. Therefore, an accurate determination of the thickness of each layer remains challenging. Here we have obtained a line profile of the intensity in the Ti edges, and used this to quantify the thickness of each layer. The procedure is shown in Fig. 8 (bottom), where the average TiO_2 layers are 2.0 ± 0.1 nm, and the average Eu_2O_3 layers are 2.2 ± 0.3 nm.

Based on the data from Fig. 8, our earlier [15] assumption about the layer interfaces being abrupt seems wrong, as this EELS data indicate that the layer interfaces are to some extent intermixed. Thus, we attempted to re-model the previous XRR data to verify this new insight. The exercise proved that there are only marginal differences between fitting the XRR data with both abrupt interfaces and with adding intermediate layer between all TiO_2 and Eu_2O_3 layers. This is probably a result of the large number of fitting parameters introduced for modelling amorphous layers and their effective density, which is different from standard densities of crystalline phases.

4. Discussion

The discussion of the effect of subnanometer structuring of TiO_2 and Eu_2O_3 on their optical properties will be divided into 4 parts: Energy transfer, Concentration quenching, Quantum confinement and structure.

4.1. Energy transfer

The luminescence spectrum of europium and its sensitization by titanium oxide in amorphous europium titanium oxides have previously been investigated as films [15,16,23–25] and powder [26–28], all showing Eu^{3+} luminescence upon excitation through the titanium oxide CT absorption. The sol-gel prepared thin films and powders by Rocha et al. [23] and Kawai et al. [28], respectively, show a change in Eu^{3+} emission spectrum upon annealing that is identical to the spectrum that we obtain for the 10-20Eu samples (Fig. 2) [23]. In both these cases and in our work, this change in emission spectrum coincides with the appearance of anatase peaks in XRD. Leroy et al. also report the same change for low concentrations (≤2.5% Eu) [25].

The energy transfer from the CT state of the $(TiO_6)^{8-}$ clusters, amorphous TiO_2 or anatase, to Eu^{3+} is well documented. When Eu^{3+} is not incorporated directly into TiO_2, the transfer efficiency should decrease with increasing TiO_2 and Eu_2O_3 layer thicknesses (*x*N samples), as excitations in the middle of TiO_2 layers would have to migrate to the TiO_2/Eu_2O_3 interface in order to transfer into the f states of Eu_2O_3. Both the decrease in the ratio of peak values of CT and f-f excitation, inset Fig. 5, and the onset of CT emission at N = 50, Fig. 2, supports this. The decay data in Fig. 4 also show that the lifetime of Eu^{3+} $^5D_0 \rightarrow {}^7F_2$ emission does not decrease enough to account for the large decrease in emission intensity. This means that the reduction in quantum yield (see Fig. 3) must come from a reduced $TiO_2 \rightarrow Eu_2O_3$ energy transfer efficiency and/or an increase in the quenching rate of the TiO_2 CT state.

4.2. Concentration quenching

Concentration quenching is a term used for the often observed decrease in luminescence efficiency with higher concentrations of optically active ions. This can come from cross-relaxation to a non-radiative state in a neighboring ion of the same or different type, or energy migration from ion to ion through the host matrix until the excitation reaches a non-radiative recombination site like a defect or impurity ion. Cross relaxation from the $^5D_0$ state to a lower energy state in a neighboring Eu^{3+} is not possible since no $^5D_0 \rightarrow {}^7F_n$ transitions match the transition energy between any states below $^5D_0$. Cross-relaxation to another excited Eu^{3+} (i.e. up conversion) is possible, but requires much higher light intensity than a Xe lamp or He–Cd laser can provide. Thus, the only source of concentration quenching in this system is by energy migration between Eu^{3+} ions to non-radiative recombination centers.

Fig. 4 shows that the lifetime of the $^5D_0$ emission do indeed decrease for *x*Eu samples with increasing Eu_2O_3 content. This is expected as the resulting Eu^{3+} concentration of even 30Eu (9.5 $\%_{cat}$ Eu^{3+}) samples is larger than what is generally used in Eu^{3+} based phosphors. The purity of our $Eu(thd)_3$ precursor is not particularly high, 99.9%, while often 99.999% chemicals are used for optical materials. Thus the amount of non-Eu lanthanide impurities is expected to be significantly higher than in high-purity phosphor materials, leading to more quenching sites. This concentration quenching explains the drop in relative quantum efficiency for higher Eu_2O_3 contents than 60Eu (Fig. 3). However, the

lifetime of the $^5D_0$ state in the layered *x*N samples do not decrease nearly as much even though they consist of layers of pure Eu_2O_3. The Eu–Eu energy migration should be high within each Eu_2O_3 layer, but energy migration between the 2D layers is not possible. The number of impurities within effective migration radius in such a 2D layer is much lower than in a 3D matrix, leading to an effectively much lower concentration of "reachable" quenching sites for the migrating Eu^{3+} excitation. Thus the concentration quenching is drastically suppressed even though the Eu^{3+} concentration is 100% and the purity is low, compared to 3D situation in the non-layered *x*Eu samples.

4.3. Quantum confinement

Fig. 5 shows how the titanate CT state is affected by TiO_2 content and layer structure. The layered *x*N samples show no variation in this peak, and neither do the *x*Eu samples for $x \leq 50$. This means that alternating TiO_2 and Eu_2O_3 cycles induces delocalization of the CT state and that higher TiO_2 content either by increasing the TiO_2/Eu_2O_3 cycle ratio or layering does not increase this any further. The peak is blue shifted for *x*Eu samples with $x \geq 60$, however, indicating that the 3D network of connected $(TiO_6)^{8-}$ is reduced. Thus, the transition from cluster-like $(TiO_6)^{8-}$ CT states to semiconductor-like delocalized TiO_2 bands is complete at 50Eu. The CT emission from the 50 N in Fig. 2 is similar to what is expected from bulk TiO_2 [29].

4.4. Structure

From the TEM data presented here it seems that the layers do not have as abrupt interfaces as we originally thought based on previous XRR measurements. The slight unevenness of the layers seen in Fig. 6 is likely also present in the electron beam direction, and could contribute to the graded composition seen in Fig. 8. However, as the layer thickness is larger than the observed unevenness, we still expect there to be a significant graded stoichiometry throughout the individual layers.

With STEM-EELS it was also possible to resolve the individual TiO_2 and Eu_2O_3 layer thicknesses. These are about 2.0 and 2.2 nm, respectively.

5. Conclusion

In this work we have investigated the possibilities for affecting the absorption, transfer, emission and quenching mechanisms by sub-nanometer sized layer structures. It is possible to drastically reduce the concentration quenching by making (sub-)nanometer layers that confine energy migration to 2D planes. The number of defects within a 2D circle is much lower than in a 3D sphere, which allows for higher defect and impurity concentrations and less pure starting chemicals. We have also shown that it is possible to transition between cluster-like to bulk-like properties of semiconductor materials by utilizing the excellent thickness resolution of ALD. In conclusion, ALD is a powerful synthesis tool that provides excellent possibilities for complex subnanometer layer structures.

Acknowledgements

This work was performed within "The Norwegian Research Centre for Solar Cell Technology" project number 193829, a Centre for Environment-friendly Energy Research co-sponsored by the Research Council of Norway and research and industry partners in Norway. The Research Council of Norway is also acknowledged for the support to the Norwegian Centre for Transmission Electron Microscopy (NORTEM), project number 197405/F50.

References

[1] C. Feldmann, et al., Inorganic luminescent materials: 100 Years of research and application, Adv. Funct. Mater. 13 (7) (2003) 511–516.
[2] J.-C. Bünzli, S. Eliseeva, Basics of lanthanide photophysics, in: P. Hänninen, H. Härmä (Eds.), Lanthanide Luminescence, Springer Berlin Heidelberg, 2011, pp. 1–45.
[3] N.C. George, K.A. Denault, R. Seshadri, Phosphors for solid-state white lighting, Annu. Rev. Mater. Res. 43 (1) (2013) 481–501.
[4] M.J. Weber, Lanthanide and actinide lasers, Lanthanide and Actinide Chemistry and Spectroscopy, American Chemical Society, 1980, pp. 275–311.
[5] A.J. Kenyon, Recent developments in rare-earth doped materials for optoelectronics, Prog. Quantum Electron. 26 (4–5) (2002) 225–284.
[6] J.-c.G. Bünzli, The europium(III) ion as spectroscopic probe in bioinorganic chemistry, Inorg. Chim. Acta 139 (1–2) (1987) 219–222.
[7] W.G. Van Sark, et al., Luminescent solar concentrators - a review of recent results, Opt. Exp. 16 (26) (2008) 21773–21792.
[8] B.M. van der Ende, L. Aarts, A. Meijerink, Lanthanide ions as spectral converters for solar cells, Phys. Chem. Chem. Phys. 11 (47) (2009) 11081–11095.
[9] C. Strümpel, et al., Modifying the solar spectrum to enhance silicon solar cell efficiency–An overview of available materials, Sol. Energy Mater. Sol. Cells 91 (4) (2007) 238–249.
[10] C. Ronda, Luminescence loss mechanisms, J. Lumin. 129 (12) (2009) 1824–1826.
[11] Q.Y. Zhang, X.Y. Huang, Recent progress in quantum cutting phosphors, Prog. Mater. Sci. 55 (5) (2010) 353–427.
[12] J. Zhou, et al., Upconversion luminescent materials: advances and applications, Chem. Rev. 115 (1) (2015) 395–465.
[13] F. Wang, et al., Tuning upconversion through energy migration in core–shell nanoparticles, Nat. Mater. 10 (12) (2011) 968–973.
[14] X. Li, et al., Successive layer-by-layer strategy for multi-shell epitaxial growth: shell thickness and doping position dependence in upconverting optical properties, Chem. Mater. 25 (1) (2013) 106–112.
[15] P.-A. Hansen, et al., Luminescent properties of multilayered Eu_2O_3 and TiO_2 grown by atomic layer deposition, Chem. Vap. Deposition 20 (2014) 274–281.
[16] P.-A. Hansen, et al., Luminescence properties of europium titanate thin films grown by atomic layer deposition, RSC Adv. 4 (23) (2014) 11876–11883.
[17] P.-A. Hansen, et al., Structural and optical properties of lanthanide oxides grown by atomic layer deposition (Ln = Pr, Nd, Sm, Eu, Tb, Dy, Ho, Er, Tm, Yb), Dalton Trans. 42 (30) (2013) 10778–10785.
[18] V. Miikkulainen, et al., Crystallinity of inorganic films grown by atomic layer deposition: overview and general trends, J. Appl. Phys. 113 (2) (2013) 021301.
[19] K.B. Klepper, et al., Atomic layer deposition of organic-inorganic hybrid materials based on saturated linear carboxylic acids, Dalton Trans. 40 (17) (2011) 4636–4646.
[20] P.-A. Hansen, et al., Luminescence properties of lanthanide and ytterbium lanthanide titanate thin films grown by atomic layer deposition, J. Vac. Sci. Technol. A: Vac., Surf. Films 34 (1) (2016) 01A130.
[21] M. Bosman, et al., Mapping chemical and bonding information using multivariate analysis of electron energy-loss spectrum images, Ultramicroscopy 106 (11) (2006) 1024–1032.
[22] M.M.J. Treacy, Z dependence of electron scattering by single atoms into annular dark-field detectors, Microsc. Microanal. 17 (6) (2011) 847–858.
[23] L.A. Rocha, et al., Eu (III) as a probe in titania thin films: the effect of temperature, Mater. Chem. Phys. 101 (1) (2007) 238–241.
[24] K.L. Frindell, et al., Sensitized luminescence of trivalent europium by three-dimensionally arranged anatase nanocrystals in mesostructured titania thin films, Angew. Chem. 114 (6) (2002) 1001–1004.
[25] C. Leroy, et al., Sol–gel technique for the generation of europium-doped mesoporous and dense thin films: a luminescent study, J. Lumin. 129 (12) (2009) 1641–1645.
[26] J. Ovenstone, et al., A study of the effects of europium doping and calcination on the luminescence of titania phosphor materials, J. Phys. Chem. B 105 (30) (2001) 7170–7177.
[27] J. Ovenstone, et al., Luminescence in europium-doped titania: Part II. High concentration range of Eu^{3+}, J. Mater. Res. 17 (10) (2002) 2524–2531.
[28] T. Kawai, A. Shimogaki, K. Kifune, Crystalline-phase dependent red luminescence of TiO_2:Eu^{3+} particles prepared by a sol–gel method, Philos. Mag. Lett. 88 (1) (2008) 1–7.
[29] L. Kernazhitsky, et al., Room temperature photoluminescence of anatase and rutile TiO_2 powders, J. Lumin. 146 (2014) 199–204.